analytical chemistry

Letter

Cite This: Anal. Chem. 2018, 90, 6362−6366

pubs.acs.org/ac

Hyperspectral Stimulated Raman Scattering Microscopy Unravels Aberrant Accumulation of Saturated Fat in Human Liver Cancer

Shuai Yan,[†,∥] Sishan Cui,[‡,∥] Kun Ke,[§] Bixing Zhao,[§] Xiaolong Liu,[§] Shuhua Yue,*[,‡] and Ping Wang*[,†]

[†]MoE Key Laboratory for Biomedical Photonics, Wuhan National Laboratory for Optoelectronics-Huazhong University of Science and Technology, Wuhan, 430074, China

[‡]School of Biological Science and Medical Engineering, Beijing Advanced Innovation Center for Biomedical Engineering, Beihang University, Beijing, 100083, China

[§]The United Innovation of Mengchao Hepatobiliary Technology Key Laboratory of Fujian Province, Mengchao Hepatobiliary Hospital of Fujian Medical University, Fuzhou, 350025, China

Supporting Information

ABSTRACT: Lipid metabolism is dysregulated in human cancers. The analytical tools that could identify and quantitatively map metabolites in unprocessed human tissues with submicrometer resolution are highly desired. Here, we implemented analytical hyperspectral stimulated Raman scattering microscopy to map the lipid metabolites in situ in normal and cancerous liver tissues from 24 patients. In contrast to the conventional wisdom that unsaturated lipid accumulation enhances tumor cell survival and proliferation, we unexpectedly visualized substantial amount of saturated fat accumulated in cancerous liver tissues, which was not seen in majority of their adjacent normal tissues. Further analysis by mass spectrometry confirmed significant high levels of glyceryl tripalmitate specifically in cancerous liver. These findings suggest that the aberrantly accumulated saturated fat may have great potential to be a metabolic biomarker for liver cancer.

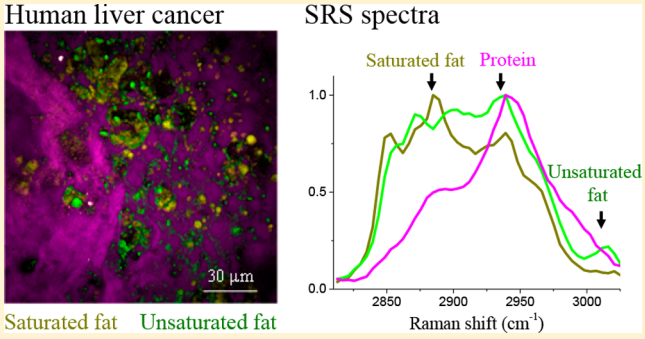

Altered metabolic activities and aberrant metabolites are crucial results of diseases, notably for most cancers.[1,2] Multiple studies have implicated that lipid desaturation and unsaturated lipid accumulation enhance tumor cell survival and proliferation.[3,4] Rysman et al. showed an increase in the degree of lipid saturation in lipogenic tumor tissues compared with nonlipogenic ones, and such an increase in lipid saturation protected cancer cells from free radicals and chemotherapeutics.[5] However, it is not clear about lipid storage or desaturation in human liver cancer.[6] This is partially due to a lack of suitable tools to quantitatively map intracellular lipid molecules in intact human tissues. For quantitative biochemical analysis, mass spectrometry is often used, but it requires a hundred milligrams of tissue for the initial homogenization and complex separation processes. Such limitation makes mass spectrometry impossible to map intracellular distribution of biomolecules of interest in intact tissues. As an optical alternative, noninvasive spontaneous Raman spectroscopy has been practical for cancer diagnosis with great analytical sensitivity.[7−9] However, slow spectral acquiring speed is persistently the weak point of spontaneous Raman, largely due to inefficient spontaneous scattering of Stokes photons. Based on enhanced stimulated emission by phase locked pulse lasers, coherent anti-Stokes Raman scattering (CARS)[10] and stimulated Raman scattering (SRS)[11] gained the Raman transition rate more than 7 orders of magnitude,[12] which offered unprecedented fast vibrational imaging for biomedical studies.[13] Single frequency CARS[14] and SRS were frequently implemented for a variety of applications with superior sensitivity, imaging speed, and contrast but lack sufficient chemical specificity to identify various types of biomolecules in complex. To enhance imaging selectivity, compound Raman, which integrated fast single-frequency SRS imaging with confocal Raman spectral analysis,[15] revealed aberrant accumulation of unsaturated fat in lipid droplets of human prostate cancer tissues.[16] In a recent advance, dual-color SRS microscopy has successfully determined brain tumor margins[17] and finally entered into the operating room for intraoperative histopathologic diagnosis and fast decision-making. However, the spectral resolution is not high enough to discriminate multiple types of biomolecules due to overlapped spectra. Multiplex,[18] hyperspectral SRS[19,20] and broadband CARS microscopy,[21] have greatly expanded the capabilities of coherent Raman for real chemical selective imaging[22,23] and been straightforward for unprocessed diseased tissue examinations. However, these potent spectral imaging tools have not been employed for assessment of tissues from human patients.

Herein, we performed hyperspectral SRS imaging of normal and cancerous liver tissues collected from 24 human patients

Received: March 23, 2018
Accepted: May 14, 2018
Published: May 14, 2018

DOI: 10.1021/acs.analchem.8b01312
Anal. Chem. 2018, 90, 6362−6366

diagnosed with hepatocellular carcinoma. Based on characteristic Raman profiles for saturated fat, unsaturated fat, protein, and lipofuscin granules, we specifically discovered aberrant accumulation of saturated fat in a large amount in cancerous liver tissues compared with that in normal liver tissues. Further study by mass spectrometry showed a significantly higher accumulation of glyceryl tripalmitate, one typical form of saturated fat, in cancerous liver tissues compared with that in normal tissues. These findings suggest that saturated fat plays a critical role in liver cancer development and could be a potential marker for liver cancer diagnosis, which breaks conventional wisdom that cancer cells survive and proliferate depending on unsaturated fat.

Figure 1a presents the molecular structures of glyceryl tripalmitate (TP) and glyceryl trioleate (TO), which are

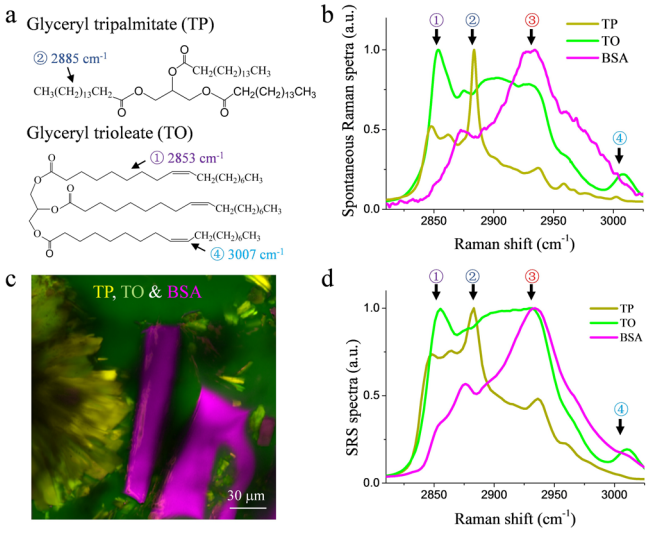

Figure 1. Hyperspectral SRS imaging of a phantom mixture of TP, TO, and BSA. (a) Chemical structures of TP and TO. (b) Spontaneous Raman spectra of them in CH region. The characteristic Raman peaks at 2853, 2885, 2935, and 3007 cm^{-1} are denoted as ①, ②, ③, and ④, respectively. (c) Multicolor image of TP, TO, and BSA obtained by hyperspectral SRS imaging and MCR reconstruction. (d) MCR optimized SRS spectra corresponding to part c.

predominant forms of saturated and unsaturated fats in cells. Figure 1b shows their corresponding spontaneous Raman spectra in CH region. As indicated by ①, Raman band peaked at 2853 cm^{-1} from symmetric CH_2 vibration stands out in the spectra of both TP (dark yellow) and TO (green) as a major vibrational band for all types of lipids. The Raman band peaked at 2885 cm^{-1}, indicated as ② in Figure 1a,b, is found in the Raman spectrum of TP only, which particularly possesses saturated straight long acyl chain.[24,25] This specific Raman band possibly originates from Fermi resonance or asymmetric vibration of CH_2 in straight and long acyl chain, such as palmitic acids comprising $(CH_2)_{14}$. In contrast to this specific Raman peak for saturated fat, Raman band at 3007 cm^{-1} (④) is corresponding to unsaturated ═CH stretch[26] in the acyl chain, which appears in spectrum of TO but not for saturated fat.[25] In addition, bovine serum albumin (BSA), which mimics protein in tissue, has a prominent Raman band of CH_3 stretching at 2935 cm^{-1} (③). The complete spontaneous Raman spectra of TP, TO, and BSA are shown in Figure S1. Although the differences among their chemical structures are subtle, Raman spectra separate them by distinct Raman bands in both fingerprint and CH vibrational regions.

We employed hyperspectral SRS microscopy (Figure S2, the setup is detailed in the Supporting Information), which obtains SRS spectra at all pixels of image with submicrometer resolution, for analytical imaging of metabolites in unprocessed human tissues. To validate the feasibility of the method, we performed hyperspectral SRS imaging of a mixture phantom that consisted of TP, TO, and BSA. Here, a hyperspectral stack of 100 images ranging from 2810 to 3025 cm^{-1} was recorded with 400 × 400 pixels at pixel dwell time of 20 μs. Despite fairly small differences among their Raman spectral profiles, the multivariate curve resolution (MCR) algorithm[27] is capable of reconstructing spatial distribution maps of TP, TO, and BSA (Figure 1c) and extracting their optimized SRS spectra (Figure 1d). In particular, SRS spectra preserved key features of all vibrational Raman bands, including 2885 cm^{-1} (②) for TP and 3007 cm^{-1} (④) for TO, and exhibited great consistence with corresponding spectra measured by spontaneous Raman (Figure 1b). Although spontaneous Raman has better spectral resolution attributed to high-performance grating and longer integration time (~10 s), hyperspectral SRS is a unique spectral imaging tool, and particularly suited for fast compositional mapping of chemicals in biological tissues. Thus, we are able to chemically identify and image saturated and unsaturated fat in biological complex by their intrinsic chemical vibrations.

After proof of concept, we obtained specimens of cancerous liver tissues and their adjacent normal tissues from 24 patients, who were diagnosed with hepatocellular carcinoma. The cancerous liver tissues were inspected by hyperspectral SRS microscopy and MCR analysis. MCR algorithm derived three prominent chemical compositions in the imaged tissue section. Figure 2c–e illustrates MCR reconstructed concentration maps of the main metabolic compositions, and their color overlay image is presented in Figure 2a for better understanding of their relative spatial distributions. As shown, we directly observed significant accumulation of two types of fats (indicated in yellow and green) in cancerous liver tissue, and their MCR decomposed SRS spectra are shown in Figure 2b. The first type of lipid composition is mapped in Figure 2c, and it existed as irregular shaped bulk and droplets. The corresponding MCR spectrum exhibited a particular strong Raman band peaked at 2885 cm^{-1}, appearing as a key feature of saturated fat (②). As a separate proof, the desaturation band at 3007 cm^{-1} (④) represented a flat profile, suggesting that there was no vibrational bond of ═CH reflected in the spectrum. For the second identified lipids, the MCR retrieved spectrum is plotted in green curve, and the corresponding concentration map is depicted in Figure 2d. The spectrum showed distinctive Raman band at 3007 cm^{-1} for unsaturated lipids as TO. Thus, we suggest that the second abundant lipids are unsaturated fat, and they are mainly stored in intracellular lipid droplets.

MCR algorithm output the third chemical composition to be protein, and the spectrum primarily comprised a CH_3 stretching mode at 2935 cm^{-1} (③ in magenta, Figure 2b). Protein distributed more evenly in the MCR reconstructed concentration map (Figure 2e), except for the locations where were occupied by saturated fat (Figure 2c).

For better understanding of composition variation, we collected SRS spectra at five different locations marked in Figure 2c,d. At specific locations of S1, S2, and S3, saturated fat was prominent owing to a significant band at 2885 cm^{-1} (②) and absent band at 3007 cm^{-1} (④) in the SRS spectra (Figure 2f). Their microscopic shapes were more close to densely packed round lipid droplets (Figure 2c). However, at locations of S4 and

DOI: 10.1021/acs.analchem.8b01312
Anal. Chem. 2018, 90, 6362–6366

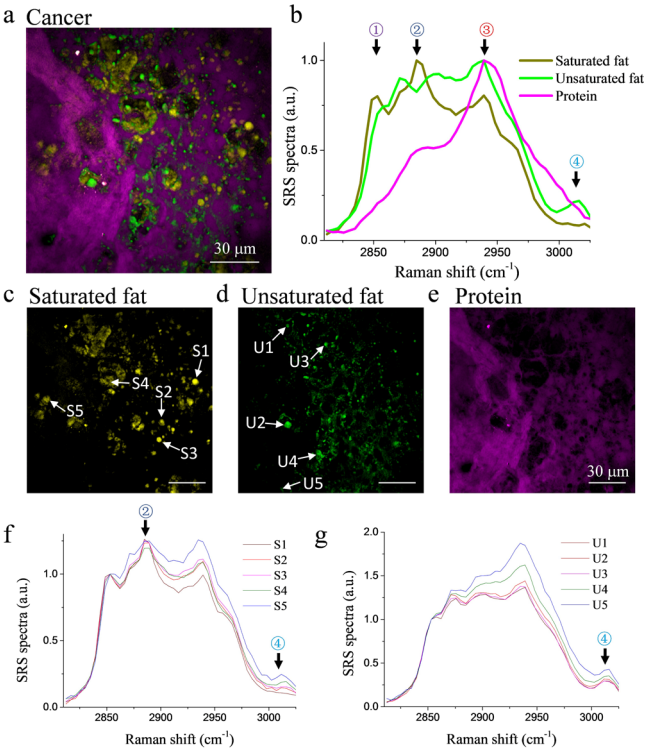

Figure 2. Hyperspectral SRS imaging of saturated and unsaturated fat in cancerous liver tissue. (a,b) Overlay image and MCR retrieved SRS spectra of saturated fat (yellow), unsaturated fat (green) and protein (magenta) in cancer tissue. (c–e) MCR reconstructed concentration maps of saturated fat, unsaturated fat and protein, respectively. (f,g) SRS spectra at indicated locations in parts c and d (normalized by intensity at 2853 cm^{-1}).

S5, the Raman band at 3007 cm^{-1} showed up independently. It implies that the lipids on those positions were mixture of both saturated and unsaturated fat. Meanwhile, from morphology, they typically had irregular shapes and existed as large sized lipid bulks in the concentration map. In the MCR reconstructed image of unsaturated fat shown in Figure 2d, we also found some extent of spectral variation at different locations. At locations of U1, U2, and U3, SRS spectra exhibit a very steady profile with prominent Raman band indicated by ④, which are characteristic of unsaturated fat (Figure 2g). With an appearance in the SRS concentration map, they were smaller with a regular round shape and potentially were lipid droplets. Nevertheless, the unsaturated fat at locations of U4 and U5 had a stronger vibrational signal at 2935 cm^{-1} in the spectra. Meanwhile, the Raman band at 3007 cm^{-1}, which represents unsaturation degree, kept almost the same intensity for all spectra. This trend suggests that protein, comprising strong CH_3 vibrational stretching (2935 cm^{-1}), may overlap with unsaturated fat spatially. To test this hypothesis, we calculated spectra differences between locations at U4, U5, and U1, and the resulting spectra were well consistent with the spectrum of BSA (Figure S3). Thus, we concluded these lipids were aggregations of lipids and protein, and they also emerged as unregularly shaped plaques shown in the SRS image (Figure 2d).

From above analytical results, hyperspectral SRS uncovered substantial amount of two types of lipids in cancerous liver tissues. Saturated fat was found abundantly in lipid droplets and they mixed with some amount of unsaturated lipids in bulks. The second resolved lipid component was unsaturated fat. They were mostly accompanied by intracellular protein.

To confirm that cancerous liver tissue indeed stored substantial more saturated fat comparing with normal liver tissue in larger area, we did hyperspectral SRS imaging of both cancerous and normal tissue with size of about 500 × 500 μm^2. In Figure 3a, 16 hyperspectral SRS images were obtained and their

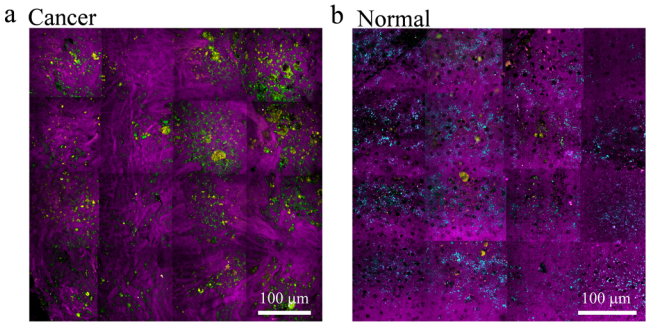

Figure 3. Comparison of cancerous and their adjacent normal liver tissues by hyperspectral SRS imaging. (a,b) Large scale images (~500 μm) of cancerous and normal tissues of patient no. 25 obtained by hyperspectral SRS imaging and MCR decomposition. Saturated fat, unsaturated fat, lipofuscin granules, and protein are colored in yellow, green, cyan, and magenta, respectively.

MCR reconstructed images were stitched to generate a mosaic large scale concentration map. In cancerous tissue, saturated fat (yellow) was widely spread (Figure S4). However, in adjacent normal liver tissue (Figure 3b), saturated fat was less spotted. In addition, we observed that liver cells in normal tissue were well organized with clear cellular morphology. Also, lipofuscin granules were frequently distributed in the examined area (Further discussion about lipofuscin granules was detailed in Supporting Information and Figure S5).

We therefore examined tissue samples from 24 patients to affirm the above findings (Table S1 and Figure S6). For each sample, we randomly selected 1–3 different locations for SRS imaging. In each location, the saturated fat was quantitated by their occupied area normalized to the total area in each MCR reconstructed image. Figure 4a shows the statistical data that the

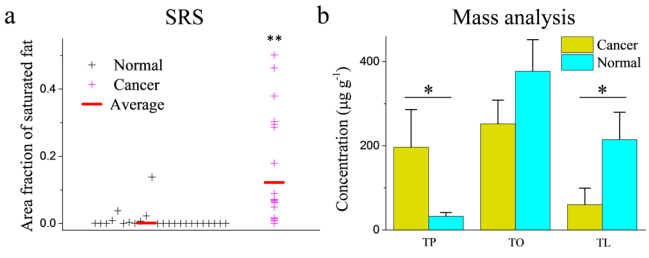

Figure 4. Saturated fat quantitation by hyperspectral SRS imaging and mass spectrometry. (a) Area fraction of saturated fat statistically measured by hyperspectral SRS imaging in normal and cancerous liver tissues from 24 patients. The average is indicated by the red line. (b) TP, TO, and TL in extracted lipids from normal and cancerous liver tissues from 11 patients measured by mass spectrometry. Error bars represent standard error of the mean.

quantified amount of the saturated fat in viewed areas in each sample. For cancerous liver tissue, we found that the averaged area fraction of saturated fat is ~12.21% in liver cancer, while only ~0.17% in the normal liver. Particularly in two patient cases, area fractions of saturated fat were up to ~40% at examined locations (Figure S7). For most normal tissues, we did not

DOI: 10.1021/acs.analchem.8b01312
Anal. Chem. 2018, 90, 6362–6366

observe saturated fat accumulation at examined locations. To validate this observation, we quantitatively analyzed both cancerous liver tissues and their normal counterparts from 11 patients by a mass spectrometer (Figure 4b). Lipids contents including glyceryl tripalmitate (TP, 16:0/16:0/16:0), glyceryl trioleate (TO, 18:1/18:1/18:1) and glyceryl trilinoleate (TL, 18:2/18:2/18:2) were extracted and quantified. Cancerous liver tissue indeed contained ~6-fold of TP than that in normal tissue. On the contrary, the levels of unsaturated lipids including TO and TL in mass data showed relatively higher in normal liver tissue (see more mass data in Figure S8). In fact, we found heterogeneity among patients and did visualize large-sized lipid droplets containing unsaturated fat in normal liver tissues from some patients (Figure S9). Because we observed unsaturated fat in both cancerous and normal liver tissues, unsaturated fat is probably not specific for cancerous tissues. However, both hyperspectral SRS imaging and mass data have found significant higher content of saturated fat specifically in cancerous live tissues than that in normal tissues, suggesting that saturated fat has a great potential to be a metabolic biomarker for liver cancer.

Different cancer types reprogram their metabolic pathways and store metabolites distinctively. By detecting intrinsic vibrational signatures of biomolecules, SRS has allowed molecular identification of aberrant metabolic accumulation in situ in unprocessed tissues of human. For a long time, fat saturation in liver cancer is rarely studied due to lack of effective tools. In this work, we found that the cancerous liver tissues from patients stored significantly higher saturated fats in lipid droplets and aggregated lipid bulks than their adjacent normal tissues. In normal liver tissues, we also chemically visualized a large amount of lipofuscin granules. With capability of chemical analysis and high-resolution imaging, metabolites alternations in cancerous lesions can be readily determined in the molecular level, which is a promise to yield new insight into cancer diagnosis and prognosis related clinical applications.

■ ASSOCIATED CONTENT

Supporting Information

The Supporting Information is available free of charge on the ACS Publications website at DOI: 10.1021/acs.analchem.8b01312.

Additional information regarding methods (PDF)

■ AUTHOR INFORMATION

Corresponding Authors

*E-mail: p_wang@hust.edu.cn.

*E-mail: yue_shuhua@buaa.edu.cn.

ORCID

Shuai Yan: 0000-0002-9083-7749

Xiaolong Liu: 0000-0002-3096-4981

Author Contributions

‖S. Yan and S. Cui contributed equally.

Notes

The authors declare no competing financial interest.

■ ACKNOWLEDGMENTS

P.W. is supported by the National Key Research and Development Program of China (Grant 2016YFA0201403), the National Natural Science Foundation of China (Grant 61675075), Science Fund for Creative Research Group of China (Grant 61421064). S. Yue acknowledges support from the National Natural Science Foundation of China (Grant 81501516) and the "Excellent Hundred Talents" Program start-up fund from Beihang University. B.Z. are grateful to the National Natural Science Foundation of China (Grant 81672376) and Natural Science Foundation of Fujian Province (Grant 2016J01417).

■ REFERENCES

(1) Warburg, O. *Science* **1956**, *123*, 309−314.

(2) Santos, C. R.; Schulze, A. *FEBS J.* **2012**, *279*, 2610−2623.

(3) Young, R. M.; Ackerman, D.; Quinn, Z. L.; Mancuso, A.; Gruber, M.; Liu, L.; Giannoukos, D. N.; Bobrovnikova-Marjon, E.; Diehl, J. A.; Keith, B.; Simon, M. C. *Genes Dev.* **2013**, *27*, 1115−1131.

(4) Li, J.; Condello, S.; Thomes-Pepin, J.; Ma, X.; Xia, Y.; Hurley, T. D.; Matei, D.; Cheng, J. X. *Cell Stem Cell* **2017**, *20*, 303−314.

(5) Rysman, E.; Brusselmans, K.; Scheys, K.; Timmermans, L.; Derua, R.; Munck, S.; Van Veldhoven, P. P.; Waltregny, D.; Daniels, V. W.; Machiels, J.; Vanderhoydonc, F.; Smans, K.; Waelkens, E.; Verhoeven, G.; Swinnen, J. V. *Cancer Res.* **2010**, *70*, 8117−8126.

(6) Schulze, A.; Harris, A. L. *Nature* **2012**, *491*, 364−373.

(7) Lattermann, A.; Matthaus, C.; Bergner, N.; Beleites, C.; Romeike, B. F.; Krafft, C.; Brehm, B. R.; Popp, J. *J. Biophotonics* **2013**, *6*, 110−121.

(8) Jermyn, M.; Mok, K.; Mercier, J.; Desroches, J.; Pichette, J.; Saint-Arnaud, K.; Bernstein, L.; Guiot, M. C.; Petrecca, K.; Leblond, F. *Sci. Transl. Med.* **2015**, *7*, 274ra19.

(9) Piredda, P.; Berning, M.; Boukamp, P.; Volkmer, A. *Anal. Chem.* **2015**, *87*, 6778−6785.

(10) Evans, C. L.; Xie, X. S. *Annu. Rev. Anal. Chem.* **2008**, *1*, 883−909.

(11) Freudiger, C. W.; Min, W.; Saar, B. G.; Lu, S.; Holtom, G. R.; He, C. W.; Tsai, J. C.; Kang, J. X.; Xie, X. S. *Science* **2008**, *322*, 1857−1861.

(12) Min, W.; Freudiger, C. W.; Lu, S.; Xie, X. S. *Annu. Rev. Phys. Chem.* **2011**, *62*, 507−530.

(13) Saar, B. G.; Freudiger, C. W.; Reichman, J.; Stanley, C. M.; Holtom, G. R.; Xie, X. S. *Science* **2010**, *330*, 1368−1370.

(14) Zumbusch, A.; Holtom, G. R.; Xie, X. S. *Phys. Rev. Lett.* **1999**, *82*, 4142−4145.

(15) Slipchenko, M. N.; Le, T. T.; Chen, H. T.; Cheng, J. X. *J. Phys. Chem. B* **2009**, *113*, 7681−7686.

(16) Yue, S.; Li, J.; Lee, S. Y.; Lee, H. J.; Shao, T.; Song, B.; Cheng, L.; Masterson, T. A.; Liu, X.; Ratliff, T. L.; Cheng, J. X. *Cell Metab.* **2014**, *19*, 393−406.

(17) Ji, M. B.; Lewis, S.; Camelo-Piragua, S.; Ramkissoon, S. H.; Snuderl, M.; Venneti, S.; Fisher-Hubbard, A.; Garrard, M.; Fu, D.; Wang, A. C.; Heth, J. A.; Maher, C. O.; Sanai, N.; Johnson, T. D.; Freudiger, C. W.; Sagher, O.; Xie, X. S.; Orringer, D. A. *Sci. Transl. Med.* **2015**, *7*, 309ra163.

(18) Fu, D.; Lu, F. K.; Zhang, X.; Freudiger, C.; Pernik, D. R.; Holtom, G.; Xie, X. S. *J. Am. Chem. Soc.* **2012**, *134*, 3623−3626.

(19) Ozeki, Y.; Umemura, W.; Otsuka, Y.; Satoh, S.; Hashimoto, H.; Sumimura, K.; Nishizawa, N.; Fukui, K.; Itoh, K. *Nat. Photonics* **2012**, *6*, 845−851.

(20) Wang, P.; Li, J.; Wang, P.; Hu, C. R.; Zhang, D.; Sturek, M.; Cheng, J. X. *Angew. Chem., Int. Ed.* **2013**, *52*, 13042−13046.

(21) Camp, C. H., Jr.; Lee, Y. J.; Heddleston, J. M.; Hartshorn, C. M.; Hight Walker, A. R.; Rich, J. N.; Lathia, J. D.; Cicerone, M. T. *Nat. Photonics* **2014**, *8*, 627−634.

(22) Camp, C. H., Jr.; Cicerone, M. T. *Nat. Photonics* **2015**, *9*, 295−305.

(23) Wei, L.; Chen, Z.; Shi, L.; Long, R.; Anzalone, A. V.; Zhang, L.; Hu, F.; Yuste, R.; Cornish, V. W.; Min, W. *Nature* **2017**, *544*, 465−470.

(24) Wu, H.; Volponi, J. V.; Oliver, A. E.; Parikh, A. N.; Simmons, B. A.; Singh, S. *Proc. Natl. Acad. Sci. U. S. A.* **2011**, *108*, 3809−3814.

(25) Rinia, H. A.; Burger, K. N.; Bonn, M.; Muller, M. *Biophys. J.* **2008**, *95*, 4908−4914.

(26) Di Napoli, C.; Pope, I.; Masia, F.; Langbein, W.; Watson, P.; Borri, P. *Anal. Chem.* **2016**, *88*, 3677−3685.

(27) Zhang, D.; Wang, P.; Slipchenko, M. N.; Ben-Amotz, D.; Weiner, A. M.; Cheng, J. X. *Anal. Chem.* **2013**, *85*, 98−106.

DOI: 10.1021/acs.analchem.8b01312
Anal. Chem. 2018, 90, 6362−6366

NOTE ADDED AFTER ASAP PUBLICATION

This paper published ASAP on May 18, 2018 with an error in the abstract graphic. The corrected paper reposted to the Web on May 21, 2018.

DOI: 10.1021/acs.analchem.8b01312
Anal. Chem. 2018, 90, 6362−6366